Avalanche criticality during compression of porcine cortical bone of different ages

Jordi Baró,[1] Peter Shyu,[2] Siyuan Pang,[3] Iwona M. Jasiuk,[2,3] Eduard Vives,[1] Ekhard K. H. Salje,[4,5] and Antoni Planes[1]

[1]*Departament d'Estructura i Constituents de la Matèria, Facultat de Física. Universitat de Barcelona, Diagonal, 647, E-08028 Barcelona, Catalonia*

[2]*Department of Bioengineering, University of Illinois, 1270 Digital Computer Laboratory, Urbana, Illinois 61801, USA*

[3]*Department of Mechanical Science and Engineering, University of Illinois, 1206 West Green Street, Urbana, Illinois 61801, USA*

[4]*Department of Earth Sciences, University of Cambridge, Downing Street, Cambridge CB2 3EQ, United Kingdom*

[5]*State Key Laboratory for Mechanical Behavior of Materials, Xi'an Jiaotong University, Xi'an 710049, China*

(Received 18 December 2015; revised manuscript received 11 April 2016; published 2 May 2016)

Crack events developed during uniaxial compression of cortical bones cut from femurs of developing pigs of several ages (4, 12, and 20 weeks) generate avalanches. These avalanches have been investigated by acoustic emission analysis techniques. The avalanche energies are power-law distributed over more than four decades. Such behavior indicates the absence of characteristic scales and suggests avalanche criticality. The statistical distributions of energies and waiting times depend on the pig age and indicate that bones become stronger, but less ductile, with increasing age. Crack propagation is equally age-dependent. Older pigs show, on average, larger cracks with a time distribution similar to those of aftershocks in earthquakes, while younger pigs show only statistically independent failure events.

DOI: 10.1103/PhysRevE.93.053001

I. INTRODUCTION

Failure of porous materials under compression has recently attracted great interest due to the intermittent and jerky response of strain to the externally applied force [1–3]. More specifically, the failure process occurs by avalanches with long sequences of failure events, which are well separated in time. Their distributions of size, energy, duration, and time intervals between events span several decades. Furthermore, these processes occur without specific length and timescales over long intervals of the event sequences, which suggests criticality of avalanches. This striking behavior seems to be a consequence of dynamical constraints imposed by the intrinsically inhomogeneous nature of this class of systems and jamming effects [4,5]. Qualitatively similar crackling noise behavior has been reported for magnetization processes [6], martensitic transitions [7,8], and plastic deformation in solids [9,10]. It has been shown that these processes share many of the characteristics of geological earthquakes. In particular, power-law distributions of energies, aftershocks, and waiting times have been reported in some cases [3,11], with statistical laws commonly used in seismic studies such as the Gutenberg-Richter's law, Omori's law, or the universal scaling law [12]. The same features were observed for all crackling noise events; we will show in this paper that the progression of damage in bones leading to their fracture falls into the same class of phenomena. In general, scale invariance has not been directly associated with specific characteristics of the microstructure. However, some studies suggest that it could be related to the distribution of elastic forces and bending moments in the case of random porous structures [13] or to the arrangement of dislocations in plasticity of small crystal volumes [14].

Avalanches in compressed porous materials are conveniently detected by measuring the acoustic emission (AE) originating from sudden changes of the internal strain field (displacement discontinuities associated with local cracks), which lead to the shrinkage of the material. AE occurs at frequencies in the range from <100 kHz to some MHz. It is a very sensitive technique capable to detect local displacements at length scales from nano- to micrometers. This technique has been widely used to monitor fracture in materials subjected to stress. The theory of AE in the case of crack initiation and propagation has been developed in Ref. [15] and for ferroelastic materials in Ref. [16].

Here, we apply the AE technique to the study of progression of failure in cortical porcine bones under a uniaxial compression. As background information we mention that bones consist of two bone types: cortical and trabecular. The cortical bone, also called a compact or dense bone, forms an outer shell of bone while the trabecular bone, also called cancellous or spongy bone, fills the inner space. Bone has a composite structure made of a soft and ductile organic phase (collagen with small amounts of other proteins) combined with a stiff and strong but brittle mineral phase (hydroxyapatite), all bathed in fluids, which also fill the pores. The cortical bone porosity ranges from few percent to about 20 percent depending on age and anatomical location. We expect that bones display a crackling noise under compression similar to other porous materials but with specific features associated with the composite structure of bone (soft and ductile collagen and strong but brittle minerals), which may influence the critical behavior. Also, as bones grow, we expect that these crackling features depend on the age of the pig. With this idea in mind we have studied cortical bones of developing pigs, ranging from very young (4 weeks) to more mature (20 weeks) ones. Pigs can live up to 20 years so a 4wk (wk) pig age corresponds to about 1 year of human age and a 20wk pig age to 6 years in terms of human age. We selected this age group based on our earlier studies on developing porcine cortical bone, which showed noticeable changes in the composition, structure, and mechanical properties of bone in this early period [17,18]. More specifically, the mineral content increases from an average of 36 weight percent (wt%) to 56 wt%, and water content (related to porosity) decreases from an average of 36 wt% to 16 wt%, while the collagen

content remains nearly unchanged at 26–28 wt% in femoral porcine cortical bone from the age of 1 to 3.5 months [17]. These compositional changes lead to an increase in elastic stiffness (Young's modulus) from mean value of 10 to 18 GPa for these two age groups [18].

Previous studies have used AE to test both trabecular (spongy) and cortical (dense) bones to monitor bone failure. It has been found that stiffness and strength of bones directly correlate with the applied strain rate [19]. Cortical bone has also been examined by AE to monitor microdamage during fatigue, although large data scatter prohibited further data analysis [20]. Numerous biomedical applications of AE analysis demonstrate its potential as a noninvasive method to determine bone state under *in vivo* conditions [21]. This includes characterization of bone healing [22] and monitoring of implants [23]. Another application is the localization of microcracks that allows to predict where fracture may subsequently occur [24]. For more information we refer the reader to the review article [25] that summarizes these developments. AE has not been applied previously to study age-related changes in failure processes of porcine cortical bone.

The collective response of the porcine cortical bones under compression is obtained from a statistical analysis of the AE events such as amplitudes, energies, durations, and waiting-times. This is the same approach as has been recently taken to study the failure of natural minerals such as goethite [26] and different sandstones [5] and some synthetic porous glasses such as Vycor and Gelsil [5] and alumina [27].

II. EXPERIMENTAL ARRANGEMENTS

A. Sample preparation

Bone samples were prepared from pig femurs harvested at 4, 12, and 20 weeks of age. They will be denoted 4wk, 12wk, and 20wk, respectively. Using a band saw, segments of cortical bone were cut from the mid-diaphysis region. After isolating the cortical bone by removing the exterior tissue and cleaning the interior with a Waterpik, rectangular prism-shaped samples were cut using a low-speed diamond wafer saw. The targeted dimensions for the samples were several millimeters, roughly 2–3 mm in widths and 5 mm in height. Samples were then stored in 50/50 vol% ethanol-phosphate-buffered solution (PBS) at -20°C. They were thawed for several hours at room temperature prior to testing.

Micro computed tomography (Micro-CT) imaging was performed on bone samples to characterize their porosity and damage. The 4-, 12-, and 20wk pig bone samples were scanned using Xradia Micro-CT (MicroXCT-400, Pleasanton, CA). Each sample was placed on the holder of Micro-CT after being dried from the PBS using tissue paper. The voltage and power of x-ray were 50 keV and 10 W, respectively. A 4X magnification with voxel size of $5 \times 5 \times 5\,\mu\text{m}^3$ was used to obtain images while rotating samples from -180 to 180 degrees. Images were taken every 0.5 degrees and there was no special filter used except one converting x-ray to digital images. The camera exposure time was 2 s. The software of "XM Controller" was used to set up scanning and obtain two-dimensional (2D) images. XM Reconstruction program was used after scanning. To offset the beam-hardening artifacts, the reading of absorption coefficient was set to be approximately

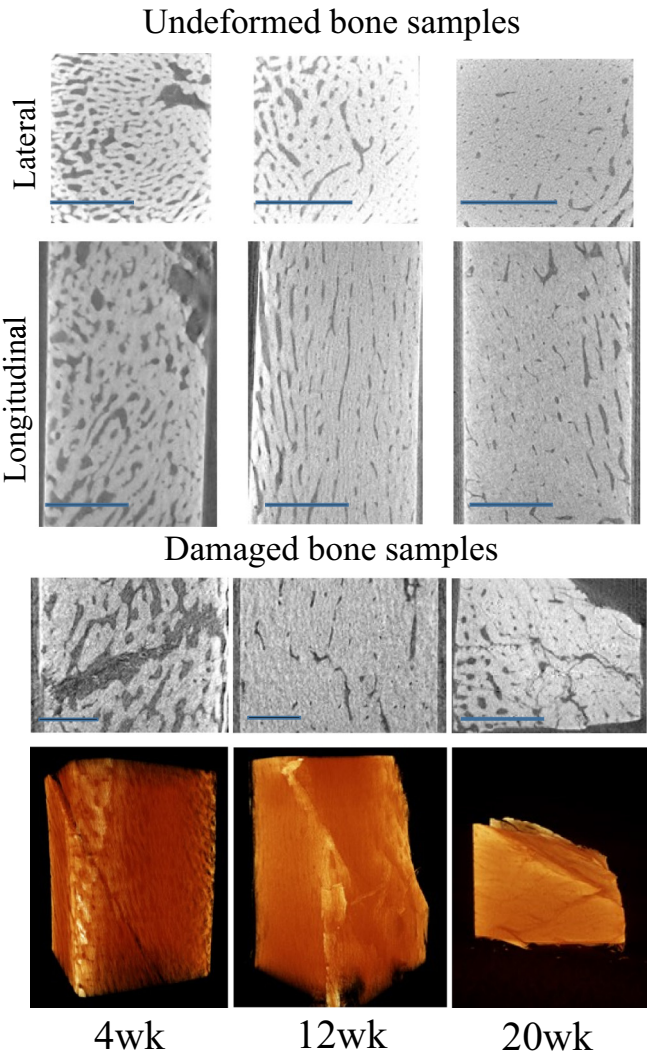

FIG. 1. Micro-CT images of 4-, 12-, and 20wk samples (using 5-μm resolution). Two top rows show select close-up slices of undeformed specimens in lateral and longitudinal planes. Third row shows 2D images of damaged specimens after loading them up to 1% strain. Images were taken in unloaded state. Length bars are 1 mm. Last row represents 3D images. Note that 12wk and 20wk specimens broke in two parts.

constant. XM 3D Viewer program converted the reconstruction file to three-dimensional (3D) images. Results are shown in Fig. 1. Undeformed images correspond to lateral and longitudinal Micro-CT sections. They show that porosity decreases with pig age, at least at the μm scale. Damaged samples were obtained by loading to 1% strain. It is interesting to note that the cracks are visible in these Micro-CT images of damaged samples without using contrast agents. In the 4wk sample a shear band is clearly observed. In 12wk and 20wk specimens failure already occurred splitting specimens into two separate pieces. 3D images of damaged samples (in orange) are shown in the bottom row of Fig. 1.

B. Compression equipment

The experimental arrangement for a uniaxial compression has been described in detail in Refs. [2,26]. Each studied

sample was placed between two parallel circular stainless steel plates, perpendicular to the direction of the applied force. The bottom plate, which hangs from the load cell at the top of the arrangement, was stationary. The upper plate could be pulled downwards by means of three guides sliding through precision ball-bearing elements, mounted on holes drilled in the bottom plate. The pulling device consisted of a water container acting as dead load. Small pump rates for the inflowing water enabled the imposition of a controlled slowly increasing load. AE was detected by piezoelectric transducers embedded in the compression plates, centered at a distance of 1 mm from the sample surface. The sensors (model Micro80 from Physical Acoustics, Princeton, NJ) were encapsulated in stainless steel in order to reduce an electrical noise. They have a broadband frequency response extending from $\leqslant$175 kHz to $\leqslant$1 MHz (maximum sensitivity of 0.3 V/mbar). A thin vaseline layer was used between the compression plate and the sensor and between the sample and the compression plate, in order to ensure a good ultrasound acoustic coupling. The signal from the sensor was preamplified to 60 dB and input in a PCI-2 system (Europhysical Acoustics, Mistras group, France) operating at 40 MHz and with a digital pass band filter of 100 kHz–2 MHz.

Avalanche analysis was performed from the recorded AE signals as follows: the beginning of an avalanche event (hit) was defined as the time t_1 at which the voltage from the transducer exceeded a predefined threshold. In our experiments this value was fixed at 27 dB. The end of the event t_2 occurred when the voltage remained below the threshold for more than a predefined hit detection time (HDT $= 100\,\mu$s). The energy E of every event was computed as the integral of the square voltage between t_1 and t_2, normalized by a reference resistance. The macroscopic compression process was monitored with the acoustic activity, dn/dt, obtained as the number n of hits (measured during intervals of 100 s) per time unit. Note that this definition of the acoustic activity is consistent with the fact that for statistical analysis purposes the process is assumed as a *point process*.

III. RESULTS AND DISCUSSION

Figure 2 shows the relative deformation, h/h_0 (h is the actual sample height and h_0 is the height before deformation), as a function of compressive stress for samples of pigs of different ages. Experiments were performed at similar low load rates $\sim$8 kPa/s. In all cases there is a tendency of samples to stiffen as stress is increased. This effect is very significant for bones of younger pigs (4wk) at the late stages of compression. The 4wk bones have highest porosity and after an early fast deformation, the pores close under the applied compressive load leading to a less porous and more stiff material. Such behavior is similar to the one of cellular material (e.g., trabecular bone) as studied by Gibson and Ashby [28]. In such porous materials, pores close under high loading, leading to a denser and stiffer material. The failure stress has been found to be strongly sample dependent, even for bone specimens of pigs of the same age, which is consistent with heterogenous nature of the bone and small size of samples as compared to pore size.

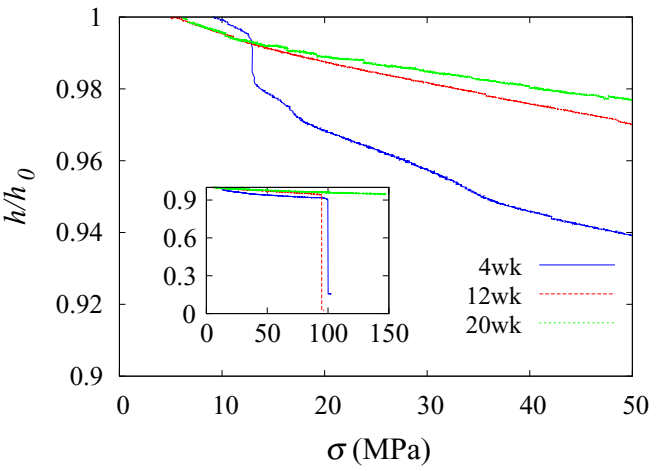

FIG. 2. Relative deformation, h/h_0, vs. compressive stress for samples of selected pig ages.

Figure 3 shows the time evolution of the AE activity (bottom panels) and of the energy of AE events (top panels) for the studied samples. Both exhibit a variable time evolution during the compression process (note that in both cases the vertical scale is logarithmic) with relatively long periods of no activity. Large part of the activity is provided by a background consisting of low-energy events ($E < 0.1$ aJ). For all samples there is a region of strong increase in the AE activity, which corresponds to the catastrophic crash region. It is worth noting that big energetic signals occur always well correlated with periods of large AE activity and, thus, these high-energy events are mainly localized in the failure region. Interestingly, AE activity is still detected after failure. This residual AE activity originates from the compression of the debris that remain after the big crash of the studied specimen. In this post-failure region only low-energy events are detected.

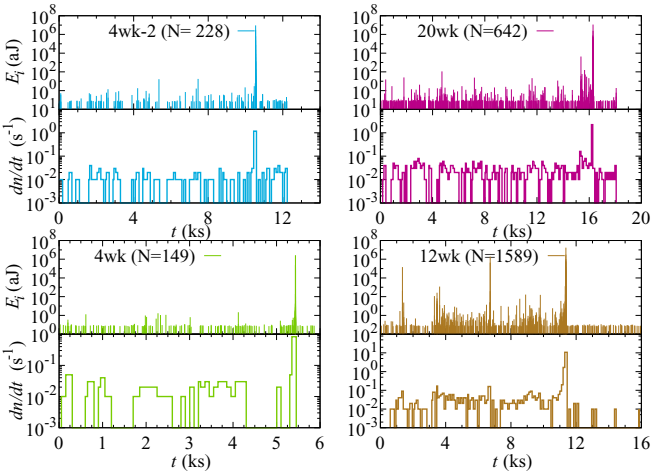

FIG. 3. Signal energy (top panels) and AE activity (bottom panels) as a function of time for samples of pigs of 4 (4wk and 4wk-2), 12 (12wk), and 20 (20wk) weeks. The activity is obtained with time intervals of 100 s. The total number of recorded signals N in each experiment is indicated in the panels.

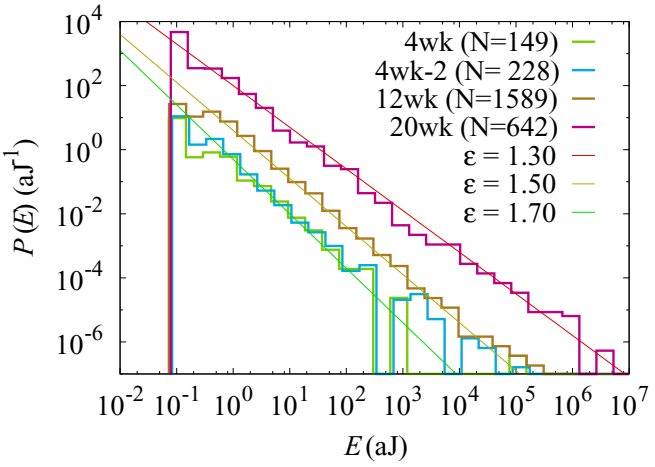

FIG. 4. Distribution of AE event energies in log-log scales for samples of pigs of 4 (4wk and 4wk-2), 12 (12wk), and 20 (20wk) weeks. The continuous lines indicate the power laws with exponents obtained from the study of maximum likelihood maps.

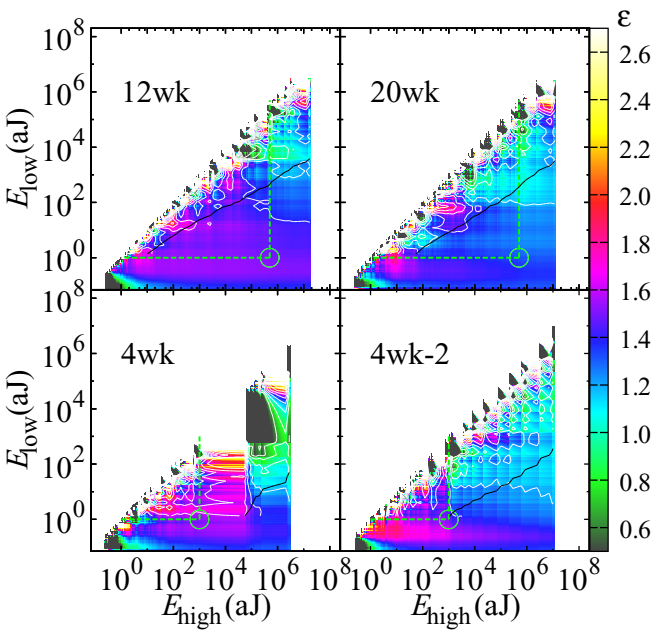

FIG. 5. Maximum likelihood maps for AE data corresponding to samples of pigs of 4 (4wk and 4wk-2), 12 (12wk), and 20 (20wk) weeks. The energy exponent that characterizes the energy distribution within the boundaries E_{low} and E_{high} is color coded. The exponent value has been chosen from data inside the green circle. See text for more details.

The distribution of energies of AE events over the full compression process has been studied for each specimen. The results show that the probability distribution of AE energies follows a power law; that is, the probability $P(E)dE$ to find an AE event within the energy interval E and $E + dE$ is described (for energies above a given lower cutoff, which is experimentally unavoidable) by

$$P(E)dE \cong CE^{-\varepsilon}dE, \tag{1}$$

where C is a normalization factor and ε is a critical exponent. The probability distributions are shown in Fig. 4 on log-log scales. A good linear behavior is observed over more than five decades for bones of younger pigs (4 weeks) and more than six for more mature pigs (12 and 20 weeks). The slope of the linear region seems to change with pig age. This would suggest that the exponent ε shows a tendency to decrease with age. This is an interesting result since it would indicate that the relative probability of large events with respect to small events increases with age in developing bones. To corroborate this behavior we have numerically estimated the critical exponent ε in more detail.

There are several ways to extract an exponent of a distribution function approaching a power-law behavior. The easiest way is to determine the slope of the linear region in a log-log plot by linear regression. However, least-square-fitting methods mostly lack accuracy because they depend on the chosen binning intervals. A very reliable method, independent of data binning, is to analyze the data with the maximum likelihood method [29]. The method provides a robust value for the exponent, its error bar, and gives an estimation for the lower reliable limit of the distribution. Recently, the use of maximum likelihood maps have been proposed where in addition to a lower bound an upper bound is included as well [30]. This upper bound is important when large events could be influenced due to device saturation effects or other reasons. We have used this method to estimate the ε exponent.

Figure 5 shows exponent maps. The exponent value is color coded and projected onto the E_{high}-E_{low} space. It represents the exponent estimated inside an interval, $E_{\text{low}} < E < E_{\text{high}}$. The maps are bounded by a minimum (E_{min}) and a maximum (E_{max}) energy value for each experiment. White contour lines serve as a guide to the eye and correspond to the exponent values labeled in the color scale. Black thick line represents a confidence threshold of the real value of the estimated exponent. The likelihood of data-points above (or left) the black line have a standard deviation larger than $\sigma = 0.1$.

The bottom-right corner of the map corresponds to the evaluation of a power-law exponent with the whole data set, but considering an upper cutoff to the distribution equal to E_{max}, instead of an open bound [29]. Fewer data points are being selected further from the bottom-right corner. Close to the bisecting diagonal $E_{\text{low}} \sim E_{\text{max}}$, the statistical error is large, rendering the estimate less reliable.

If the data are scale-free (power-law distributed) within a certain range, a plateau of constant exponent (homogeneous color, free of contour lines) will appear inside the map, and the corresponding exponent value can be given with an error ± 0.1 if it is found below the black line. The power-law hypothesis can be corroborated by evaluating the p value of each estimation using a Kolmogorov-Smirnov test. In this evaluation the value of the exponent fitted with the maximum likelihood method is forced, which yields an overestimation of the p value [31]. Considering this bias, we propose to choose p values of acceptance and rejection thresholds at 0.5 and 0.05, respectively.

The exponent maps indicate a good agreement to a power-law hypothesis (see Fig. 5) for pig ages of 12 and 20 weeks and energies between 1 and 5×10^5 aJ, shown as dashed green lines in Fig. 5. The circle at the intersection of these

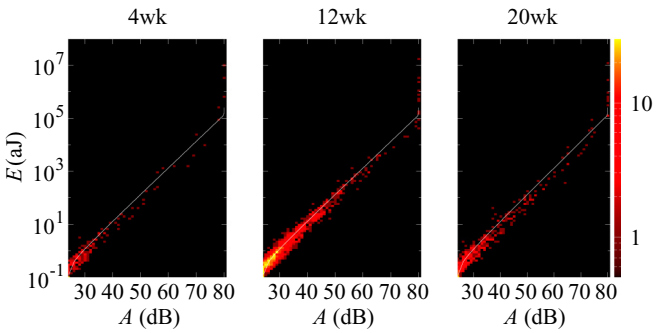

FIG. 6. Signal energy vs. signal amplitude maps corresponding to sample 12wk. The continuous line indicates the behavior $E \sim A^2$. The energy-color scale is indicated.

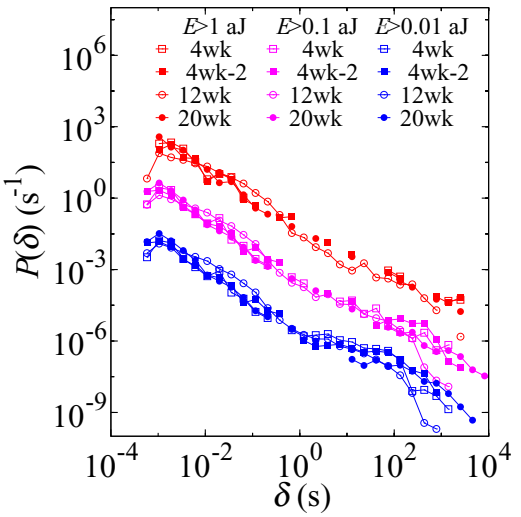

FIG. 7. Nonscaled representation of the waiting times with threshold fixed at $E > 0.01$ aJ, $E > 0.1$ aJ, and $E > 1$ aJ for AE data corresponding to samples of pigs of 4 (4wk and 4wk-2), 12 (12wk), and 20 (20wk) weeks. For the sake of clarity curves corresponding to $E > 0.1$ aJ and $E > 1$ aJ have been shifted upwards two decades.

lines indicates the region where an exponent corresponding to the whole range of values displaying power law behavior was chosen. We have checked that the corresponding p value satisfies the acceptance criteria previously discussed. Thus, in Fig. 5 we found exponents $\varepsilon = 1.30 \pm 0.10$ for 20wk bones and $\varepsilon = 1.50 \pm 0.10$ for 12wk bones. Results for 4-week-old pigs are more difficult to analyze by the power law.

For 4wk bones, Fig. 5 shows that the exponent tends to increase for high energies, suggesting a behavior better fitted by an exponential or stretched-exponential probability distribution. However, a flat plateau can also be found below 10^3 aJ, consistent with the range of power-law behavior shown in Fig 4. The obtained p value is consistent with the power-law hypothesis in the interval 1–10^3 aJ for the two studied samples of 4wk bones. The estimated exponent is then $\varepsilon = 1.70 \pm 0.10$. In Fig. 4 we have plotted straight lines with slopes corresponding to the estimated exponents. It is clear that the results fit very well the corresponding energy distributions.

Our exponents are within the same range of values found for energy exponents in other porous materials such as several minerals and Vycor—a synthetic porous SiO_2 glass [5]. The change of the energy exponent with pig age is a surprising result. One could have expected that the universality class is the same regardless of the pig age. The reported change of the power law suggests that the measured exponents are *effective exponents* influenced by some other effect induced by development.

In general, it is interesting to study whether the energy exponent evolves during the crackling process. In our case this analysis is difficult due to lack of statistics associated with the relatively low number of recorded AE events. For the sample 12wk we have checked that the same exponent is obtained with signals detected during the early stages of the process ($t < 11120$ s) and with signals detected during the crash period (11120 s $< t <$ 11370 s). These results suggest that similarly to compressed Vycor [3], there is no evolution of the exponent over successive subperiods. This is an interesting aspect taking into account the nonstationary behavior of the AE activity, which is not general in crackling noise processes [32].

We now analyze the relationship between the energy E and the maximum amplitude A of AE events. The two quantities are not statistically independent but satisfy the relation $E \sim A^2$ (Fig. 6). This result is independent of the pig age and indicates that high-energy events are associated with large amplitude signals.

Taking into account that the AE activity is nonstationary and displays relatively long silent periods, it is interesting to analyze in detail the statistics of waiting times between AE events. In Fig. 7 we have plotted a log-log representation of the waiting times distribution for all samples. The waiting time δ is given as the time between successive events defined after selecting given energy thresholds E_m. That is, $\delta_j = t_j - t_{j-1}$, with j labeling only the events with energy larger than E_m. The results indicate that all samples show very similar behavior regardless of the selected threshold. Interestingly, the waiting times span over almost six orders of magnitude in all cases. The distribution follows a reasonably good power-law decay. A small decrease of the probability is observed for all samples for waiting times in the range between 0.1 and 1 s.

It has been suggested that the waiting-time distribution is governed by the mean event rate activity, $\langle r \rangle$, which is the inverse of the mean waiting time, $\langle \delta \rangle^{-1}$ [33]. This allows a better comparison of the shape of the distributions by rescaling the axes with the mean activity rate as $\delta/\langle\delta\rangle$ $(=x)$ and $P(\Delta t)\langle\delta\rangle$, where $\langle\delta\rangle$ (function of E_m) is the mean waiting time between events with energy larger than E_m. For a homogeneous Poisson process with constant activity rate, the corresponding scaling function $\Phi(x)$ would show an exponential behavior $[\Phi(x) = e^{-x}]$. In the case of a nonhomogeneous Poisson process the exponential decay for large arguments x is expected to transform to a power-law decay [3]. Therefore, $\Phi(x)$ should be flat for low x in a log-log plot and decay linearly for large arguments due to the distribution of background activity rates. $\Phi(x)$ is expected to display a double power-law behavior if correlations exist and the process is non-Poisson. Here the scaling function exhibits a power-law behavior with a small exponent instead of being flat for low x.

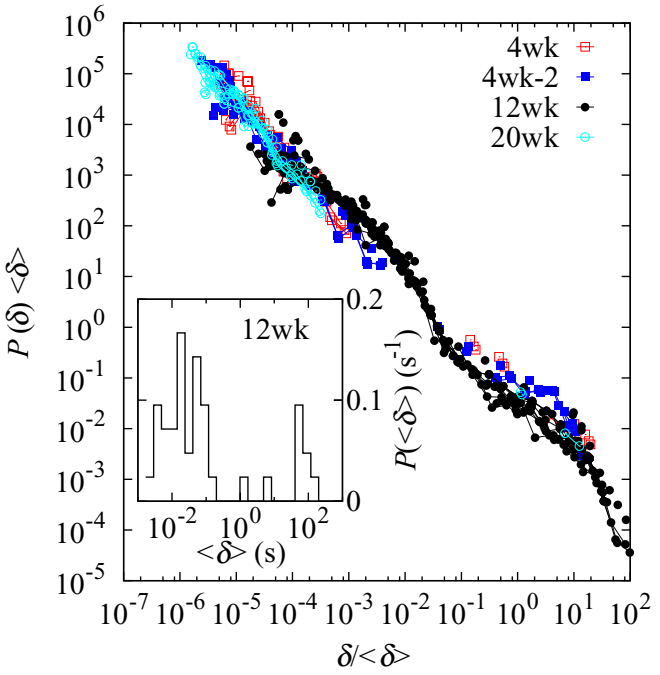

FIG. 8. Same data as described in the caption of Fig. 7 represented after scaling with the rate, for thresholds increasing by a factor 2 and starting at $E = 0.01$ aJ. The inset gives the distribution of AE rates averaged over 50 successive events for AE data corresponding to the sample 12wk.

Figure 8 shows the collapse of the data into a single curve to a very good approximation. Our data do not scale in a double power-law function as expected and intermediate values of the scaled variable $x = \delta/\langle\delta\rangle$ are very sparse. This behavior seems to be a consequence of a bimodal rate distribution. The bimodal distribution for the 12wk sample (measurement with a large number of detected AE signals) is shown in the inset of Fig. 8 (for other samples the analysis indicates also a similar distribution but it is less reliable due to a lack of statistics). The bimodal behavior could be associated with a mode switching between two activity modes [34]. Note that the highest rates occur in the collapse region.

To gain a deeper understanding about these correlations we have analyzed the time series using the Bi-test method which is especially adequate to separate effects arising from the nonstationary behavior from endogenous or intrinsic time correlations. The procedure was introduced to detect deviations from uncorrelated Poisson processes [11,35]. The time distance to the closest event (forwards and backwards in time) $\Delta_k = \min[t_k - t_{k-1}; t_{k+1} - t_k]$ and the time distance d_k to the second event in the same temporal direction, i.e., $d_k = t_{k-1} - t_{k-2}$ if $\Delta_k = t_k - t_{k-1}$ or $d_k = t_{k+2} - t_{k+1}$ if $\Delta_k = t_{k+1} - t_k$, are first determined. From data pairs, (Δ_k, d_k), the statistical variable $H_k = \Delta_k/(\Delta_k + d_k/2)$, which takes values between 0 and 1, is then build. If the analyzed time series is locally Poissonian, the values Δ_k and d_k will be statistically independent. In this case it is easy to see that H_k would be uniformly distributed [with probability $p(H) = 1$ for $0 < H < 1$], with mean value $\langle H\rangle = 1/2$.

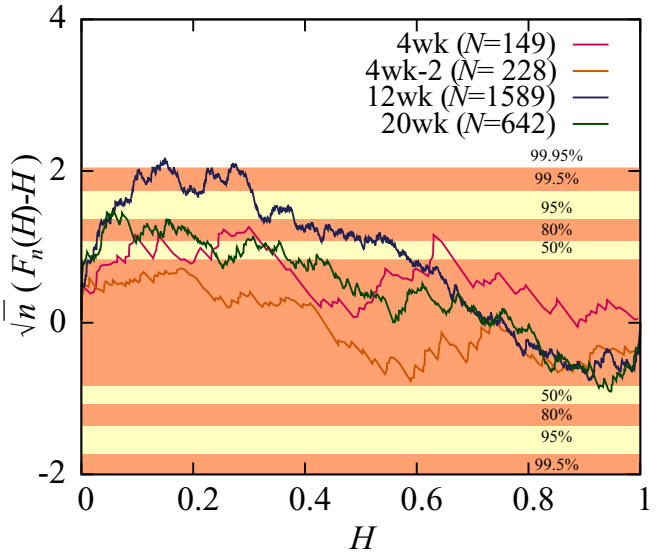

FIG. 9. Kolmogorov-Smirnoff test of uniformity of the variable H obtained from the Bi-test analysis of the AE signals corresponding to samples of pigs of 4 (4wk and 4wk-2), 12 (12wk), and 20 (20wk) weeks. The colored horizontal bands show rejection probabilities of the local Poisson hypothesis.

Deviations from the uniform distribution indicate the existence of correlations or clustering effects. The existence of an excess of low and high values of H in the distribution $p(H)$ should be understood in the sense that large periods of silence between groups of clustered events exist. On the other hand, an excess over values close to $2/3$ indicates the occurrence of some ordering where Δ is systematically smaller than $2d$. Note that this can be understood by taking into account that for events spaced almost regularly in time, $\Delta \sim d$ (for all k) and thus H would be distributed sharply around $2/3$.

Non-Poisson behavior is quantified by the Kolmogorov-Smirnov test comparing the experimental cumulative distribution function $F_n(H)$ to the expected uniform cumulative distribution function of a uniform random variable [$F(H) = H$]. This is shown in Fig. 9 for all samples. The curves show the distance between $F_n(H)$ and $F(H) = H$ as a function of H and are scaled by the colored regions that indicate the probability of the corresponding distance in a Poisson process (rejection p value). Curves reaching regions with very high rejection p value (>0.8) indicate that the studied process is unlikely to be Poissonian while curves with low rejection p value comply with the Poisson hypothesis. The obtained curves are quite flat in the case of young pigs (4wk), suggesting a behavior close to a Poisson process. Nevertheless, for bones of more mature pigs the curves display a more significant sinusoidal-like shape, which denote an excess of statistics in the regions of low and high values of H thus indicating non-Poisson behavior. This means that in this case big events induce crack-avalanches of lower magnitude in the same way that big earthquakes are followed by aftershocks, which decay following Omori's law [36].

Mechanical properties of biological and related bioinspired materials are difficult to determine from standard protocols in materials science due to sample heterogeneity that leads

to a highly variable mechanical behavior [37]. We suggest that the analysis of AE during mechanical testing provides an additional tool to suitably characterize this class of complex materials. Bone is an example of such a strongly heterogeneous material. Bone, among its other functions, provides the structural support for soft tissues. Thus, its mechanical properties are important for body's function. Bone fracture is an outstanding clinical problem. Understanding of fracture mechanisms and bones resistance to fracture can lead to better assessment of bone diseases, characterized by bones' susceptibility to fracture, and can help to design more effective treatments. Moreover, such information may be relevant to characterize bone scaffolds and help to assess regenerated bone. This paper addresses young porcine bones. Since porcine bone biology is similar to human bone, these findings may provide new insights into failure and fracture of children's bone. Present results show that in spite that failure stress is strongly sample dependent the exponent that characterizes the distribution of AE event energies systematically depends on pig age.

Our results suggest that bones become stiffer and stronger with age. This interpretation is consistent with experimental results on the development of porcine cortical bone [17,18,38,39], where bone hardness, stiffness, and strength also increase with age. These mechanical property changes are correlated with an increase in the mineral content and a decrease in bone porosity with age. This interpretation also agrees with recent results [40], which show that impact force propagation into a granular material depends strongly on the hardness of the grains constituting the material. For hard grains, the transmission occurs along chainlike paths, which suggest strong correlations and the possibility of high-energy avalanches. In contrast, for soft grains, the force propagation gives rise to a dense structure constituted of small, interconnected steps.

This study has some limitations. In our analysis we did not investigate in detail how the bone microstructure contributes to the recorded AE events. Bone has a highly complex hierarchical structure with spatially varying mineral content and porosity occurring at different structural scales. Bone failure, which consists of plasticity, damage, and fracture, is a multiscale phenomenon. Initial crack progresses along different structural scales: atomic scale (breaking of interatomic bonds), nanoscale (mineralized collagen fibril), submicroscale (single lamella), microscale (lamellar bone: osteonal and interstitial), mesoscale (cortical bone), and macroscale (whole bone). Examples of failure mechanisms include plastic slipping at crystal-collagen interfaces, cracks crossing over lamellar structures, crack deflections at cement lines surrounding osteons, and other complex processes [41]. One possible simplified approach could involve a correlation of fractal dimension of bone with bone strength. Several studies have addressed measurement of fractal dimensions of cortical bone based on its porosity [42,43]. Such analysis of cortical bone as a function of age is outside of the scope of the current study.

IV. CONCLUSIONS

We have studied how the statistical distributions of energy and waiting times during uniaxial compression of cortical femoral bones of pigs depend on the age of the pig. In particular, we have found that the critical exponent that characterizes the distribution of AE event energies decreases with pig age, which reflects the fact that large events can occur with larger probability in more mature pigs than in younger pigs. Events are not correlated for younger pigs, however; these correlations develop with age. We suggest that the increase of such correlations with increasing pig age is responsible for the apparent increase of the energy exponent.

ACKNOWLEDGMENTS

The group from Barcelona acknowledges financial support from CICyT (Spain), Projects No. MAT2013-40590-P and No. MAT2015-69777-REDT. E.K.H.S. is grateful to EPSRC for support under Grant No. EP/K009702/1. I.J. gratefully acknowledges support from the National Science Foundation (NSF) the DMR Program Grant No. 15-07169. The findings, conclusions, and recommendations expressed in this manuscript are those of the authors and do not necessarily reflect the views of the NSF.

[1] J. Davidsen, S. Stanchits, and G. Dresen, Phys. Rev. Lett. **98**, 125502 (2007).
[2] E. K. H. Salje, D. E. Soto-Parra, A. Planes, E. Vives, M. Reinecker, and W. Schranz, Philos. Mag. Lett. **91**, 554 (2011).
[3] J. Baró, A Corral, X. Illa, A. Planes, E. K. H. Salje, W. Schranz, D. E Soto-Parra, and E. Vives, Phys. Rev. Lett. **110**, 088702 (2013).
[4] E. K. H Salje and K. A. Dahmen, Annu. Rev. Condens. Matter Phys. **5**, 233 (2014).
[5] G. F. Nataf, P. O. Castillo-Villa, J. Baró, X. Illa, E. Vives, A. Planes, and E. K. H. Salje, Phys. Rev. E **90**, 022405 (2014).
[6] G. Durin and S. Zapperi, in *The Science of Hysteresis*, edited by G. Bertotti and I. Mayergoyz, Vol. II (Academic Press, San Diego, 2006), pp. 181–267.
[7] E. Vives, J. Ortín, L. Mañosa, I. Ràfols, R. Pérez-Magrané, and A. Planes, Phys. Rev. Lett. **72**, 1694 (1994).
[8] M. C. Gallardo, J. Manchado, F. J. Romero, J. del Cerro, E. K. H. Salje, A. Planes, E. Vives, R. Romero, and M. Stipcich, Phys. Rev. B **81**, 174102 (2010).
[9] F. F. Csikor, C. Motz, D. Weygand, M. Zaiser, and S. Zapperi, Science **318**, 251 (2007).
[10] J. Weiss, T. Richeton, F. Louchet, F. Chmelik, P. Dobron, D. Entemeyer, M. Lebyodkin, T. Lebedkina, C. Fressengeas, and R. J. McDonald, Phys. Rev. B **76**, 224110 (2007).
[11] J. Baró, J. M. Martn-Olalla, F. J. Romero, M. C. Gallardo, E. K. H. Salje, E. Vives, and A. Planes, J. Phys. Condens. Matter **26**, 125401 (2014).
[12] A. Corral, Physica A **340**, 590 (2004).
[13] A. H. W. Ngan, Proc. R. Soc. A **461**, 1423 (2005).

[14] R. Gu and A. H. W. Ngan, J. Mech. Phys Solids **61**, 1531 (2013).
[15] M. V. Lysak, Eng. Fract. Mech. **47**, 873 (1994); **55**, 443 (1996).
[16] E. K. H. Salje, X. Wang, X. Ding, and J. Sun, Phys. Rev. B **90**, 064103 (2014).
[17] R. Rasoulian, A. Raeisi Najafi, M. Chittenden, and I. Jasiuk, J. Biomechanics **46**, 1689 (2014);
[18] M. Chittenden, A. Raeisi Najafi, J. Li, and I. Jasiuk, J. Mech. Med. Biol. **15**, 1550074 (2015).
[19] J. Wells and R. Rawlings, Biomaterials **6**, 218 (1985).
[20] S. Agcaoglu and O. Akkus, J. Biomech. Eng. **135**, 081005 (2013).
[21] S. Shrivastava and R. Prakash, J. Biomed. Sci. Eng. **2**, 144 (2009).
[22] Y. Watanabe, S. Takai, Y. Arai, N. Yoshino, and Y. Hirasawa, J. Orthopedic Res. **19**, 548 (2001).
[23] Z. Ossi, W. Abdon, R. L. Reuben, and R. J. Ibbetson, J. Eng. Med. **227**, 1237 (2013).
[24] J. O'Toole, L. Creedon, J. Hession, and G. Muir, J. Biomech. Eng. **135**, 011006 (2013).
[25] M. Browne, A. Roques, and A. Taylor, J. Strain Analysis **40**, 59 (2005).
[26] E. K. H. Salje, G. I. Lampronti, D. E. Soto-Parra, A. Planes, and E. Vives, Am Min. **98**, 609 (2013).
[27] P. O. Castillo-Villa, J. Baró, A. Planes, E. K. H. Salje, P. Sellappan, W. M. Kriven, and E. Vives, J. Phys.:Condens. Matter **25**, 292202 (2013).
[28] L. J. Gibson and M. F. Ashby, *Cellular Solids: Structure and Properties* (Cambridge University Press, Cambridge 1999).
[29] A. Clauset, C. Rohilla-Shalizi, and M. E. J. Newman, SIAM Rev. **51**, 661 (2009).
[30] J. Baró and E. Vives, Phys. Rev. E **85**, 066121 (2012).
[31] A. Deluca and A. Corral, Acta Geophys. **61**, 1351 (2013).
[32] M. A. Lebyodkin, N. P. Kobolev, Y. Bougherira, D. Entemeyer, C. Fressengeas, V. S. Gornakov, T. A. Lebyodkina, and I. V. Shashkov, Acta mater. **60**, 3729 (2012).
[33] P. Bak, K. Christensen, L. Danon, and T. Scanlon, Phys. Rev. Lett. **88**, 178501 (2002).
[34] Y. Ben-Zion, K. Dahmen, V. Lyakhovsky, D. Ertas, and A. Agnon, Earth Planet. Sci. Lett. **172**, 11 (1999).
[35] H. Bi, G. Börner, and Y. Chu, Astron. Astrophys. **218**, 19 (1989).
[36] T. Utsu, Y. Ogata, and R. S. Matsu'ura, J. Phys. Earth **43**, 1 (1995).
[37] C. Hellmich and D. Katti, MRS Bulletin **40**, 309 (2015).
[38] L. Feng and I. Jasiuk, J. Biomech. **44**, 313 (2010).
[39] L. Feng, M. Chittenden, J. Schrirer, M. Dickinson, and I. Jasiuk, J. Biomech. **45**, 1775 (2012).
[40] A. H. Clark, A. J. Petersen, L. Kondic, and R. P. Behringer, Phys. Rev. Lett. **114**, 144502 (2015).
[41] F. Sabet, A. Najafi Raeisi, E. Hamed, and I. Jasiuk, Interface Focus **6**, 20150055 (2016).
[42] L. Deseri, M. Di Paola, M. Zingales, and P. Pollaci, Int. J. Numer. Meth. Biomed. Engng. **29**, 1338 (2013).
[43] D. Sánchez-Molina, J. Velázquez-Ameijide, V. Quintana, C. Arregui-Dalmases, J. R. Crandall, D. Subit, and J. R. Kerrigan, Med. Eng. Phys. **35**, 576 (2013).